Attosecond x-ray free-electron lasers utilizing an optical undulator in a self-selection regime

Xinlu Xu,[1,2,*] Jiaxin Liu,[1] Thamine Dalichaouch,[3,4] Frank S. Tsung,[3] Zhen Zhang,[5] Zhirong Huang,[5] Mark J. Hogan,[5] Xueqing Yan,[1,2,6] Chan Joshi,[4] and Warren B. Mori[3,4]

[1]*State Key Laboratory of Nuclear Physics and Technology, and Key Laboratory of HEDP of the Ministry of Education, CAPT, Peking University, Beijing 100871, China*

[2]*Beijing Laser Acceleration Innovation Center, Beijing 100871, China*

[3]*Department of Physics and Astronomy, University of California Los Angeles, Los Angeles, California 90095, USA*

[4]*Department of Electrical Engineering, University of California Los Angeles, Los Angeles, California 90095, USA*

[5]*SLAC National Accelerator Laboratory, Menlo Park, California 94025, USA*

[6]*Collaborative Innovation Center of Extreme Optics, Shanxi University, Shanxi 030006, China*

(Received 5 May 2023; accepted 29 November 2023; published 17 January 2024)

Accelerator-based x-ray free-electron lasers (XFELs) are the latest addition to the revolutionary tools of discovery for the 21st century. The two major components of an XFEL are an accelerator-produced electron beam and a magnetic undulator, which tend to be kilometer-scale long and expensive. A proof-of-principle demonstration of free-electron lasing at 27 nm using beams from compact laser wakefield accelerators was shown recently by using a magnetic undulator. However, scaling these concepts to x-ray wavelengths is far from straightforward as the requirements on the beam quality and jitters become much more stringent. Here, we present an ultracompact scheme to produce tens of attosecond x-ray pulses with several GW peak power utilizing a novel aspect of the FEL instability using a highly chirped, prebunched, and ultrabright tens of MeV electron beam from a plasma-based accelerator interacting with an optical undulator. The FEL resonant relation between the prebunched period and the energy selects resonant electrons automatically from the highly chirped beam which leads to a stable generation of attosecond x-ray pulses. Furthermore, two-color attosecond pulses with subfemtosecond separation can be produced by adjusting the energy distribution of the electron beam so that multiple FEL resonances occur at different locations within the beam. Such a tunable coherent attosecond x-ray sources may open up a new area of attosecond science enabled by x-ray attosecond pump/probe techniques.

DOI: 10.1103/PhysRevAccelBeams.27.011301

Coherent attosecond pulses have significantly advanced modern science by allowing steering and tracking of electronic motion on an unprecedentedly fast time scale [1–6]. Many of these achievements are based on high-harmonic generation (HHG) sources [7–9] that emit photons with energies tens of times that of the driving laser photon energy when it interacts with rare gases. Recently, even higher energy photons have been generated by another HHG mechanism by firing relativistic $\gtrsim 10^{18}$ W/cm^2 laser pulses at a solid surface [10]. However, the conversion efficiency of the HHG photons tends to be low in the soft and hard x-ray regime, thereby limiting the range of applications of these HHG sources. On the other hand, x-ray free-electron lasers (XFELs) based on kilometer long radio-frequency (rf) accelerators [11–13] has demonstrated the generation of intense hundreds of attosecond x-ray pulses in hundreds of meters long magnetic undulator [14].

Plasma-based accelerator (PBA) [15–18] can deliver high-energy electrons in millimeter to centimeter long plasmas. Recently, how to build XFELs using compact PBAs instead of kilometer long rf accelerators is very active [19] and many advances have been made including the proof-of-principle lasing experiments in the ultraviolet from an electron beam produced in PBA propagating in a magnetic undulator [20–24]. However, there are many uncertainties to scale the current configuration where the beam propagates through a transport line into a magnetic undulator to x-ray region since a XFEL has much more

*xuxinlu@pku.edu.cn

Published by the American Physical Society under the terms of the Creative Commons Attribution 4.0 International license. Further distribution of this work must maintain attribution to the author(s) and the published article's title, journal citation, and DOI.

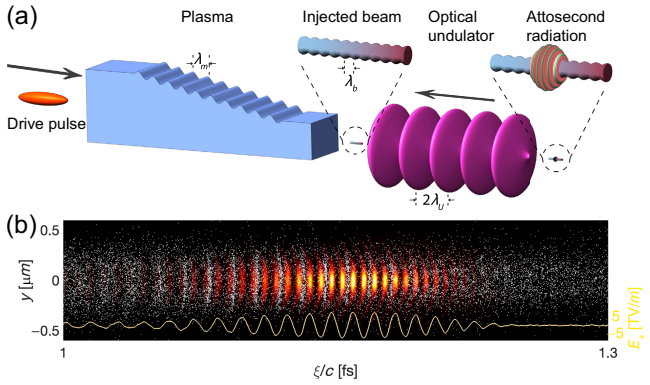

FIG. 1. Illustration of attosecond pulse generation. (a) An electron beam driver propagates through a density modulated plasma downramp to inject a prebunched, highly chirped, and ultrabright electron beam that collides with a laser pulse at the exit of the plasma to generate an attosecond pulse. (b) PIC simulation results: Beam energy 1 GeV, peak current 34 kA, upper/lower shelf plasma density $2.17/1.97 \times 10^{19}$ cm^{-3}, ramp length 60 μm, plasma density modulation period 400 nm and amplitude 3.94×10^{16} cm^{-3}. The electrons bunching (white dots) on the x-ray radiation scale, the radiation intensity E_x^2 (black-red-yellow) at $x = 0$ plane and the on-axis electric field (yellow line) when it saturates ($z = 10\lambda_U$).

stringent requirements on the beam quality and stability than current PBA can deliver. Although recent controllable injection schemes of plasma accelerators can generate high-quality beam inside the plasma [25–28], it is not clear whether their quality can be maintained after the transport line when considering various jitters [29].

In this article, we propose a radically different ultra-compact XFEL concept, depicted in Fig. 1, that is based on an unexplored regime enabled by PBA and an optical undulator. This concept can generate tens of attosecond x-ray pulses with several GW power while tolerating large fluctuations of the beams from PBA. There are several key features that distinguish this concept from other conventional or PBA-based XFEL concepts [20,21,24]. First, we propose prebunching a highly chirped electron beam on an x-ray wavelength scale in the PBA. Due to the huge acceleration gradients in PBA, the injected beam can be characterized by tens of MeV/fs energy chirp, i.e., the electron's energy strongly depends on its axial phase within the plasma wake. When a prebunched beam with a large energy chirp oscillates inside an undulator, the electrons with resonant energy at the bunching wavelength radiate coherently [30] while electrons at other energies begin emitting photons at a much lower fluctuation level. As a result, only a small portion of the beam radiates a fully coherent attosecond pulse with a stable energy and spectrum, which is in contrast to the ultrafast pulses generated from XFELs [14,31,32] in the self-amplified spontaneous emission mode whose pulse energy and spectrum fluctuate significantly. Second, we also propose the use of a powerful, subpicosecond class laser pulse as an optical undulator [33,34]. An undulator wavelength of a few microns reduces the resonant energy of the electron beam needed to produce x-rays from a few GeV to sub-100 MeV, and the direct collision of the electron beam with the undulator laser pulse eliminates the need to have a complex electron beam transport line to match the beam from the plasma to the magnetic undulator [20,21] without significant degradation of the beam quality [35,36]. Finally, the ultrahigh brightness beam allows the FEL instability to grow rapidly within an undulator wavelength and the radiation saturates before the beam diffracts significantly. The distance over which the radiation power grows by a factor of e (also known as gain length) is comparable to the undulator wavelength, which is orders of magnitude shorter than possible in conventional XFELs [11–14,31,32]. The self-selection mechanism of this novel FEL instability can tolerate tens of MeV energy jitter of the beams while the use of an optical undulator without transverse focusing can accept beams with tens of degrees pointing jitter and tens of micron transverse position jitter. In PBA, there can be large jitters to the electron beam characteristics, thus these tolerances are critical for the stable operation of the radiation source. The proposed scheme provides a compact and inexpensive solution for generating coherent x-rays with a ∼10 Hz repetition rate which may be improved to MHz in the future [37].

Additionally, attosecond harmonic pulses can be generated with subfemtosecond temporal separation by different parts of the chirped beam if its energy range covers the resonant energies of harmonics. These synchronized pulses can be used as multiple probes with different colors or enable attosecond pump/probe experiments, thus greatly broadening the application range of the proposed concept.

To demonstrate the new physics of the proposed PBA-based XFEL, we use the three-dimensional (3D) particle-in-cell (PIC) code OSIRIS [38] with recently developed high-fidelity Maxwell solvers [39,40] to model each of the three components of the concept described above including the collision of highly chirped, prebunched, and ultrabright electron beam, self-consistently produced in a PBA stage, with an optical undulator (see Appendix A for simulation setup). The concept utilizes an extremely bright beam, leading to a very large FEL amplification bandwidth, and this together with the large energy chirp and strong space charge effects, leads to an XFEL regime that cannot be described with the standard FEL theory or let alone modeled with standard FEL codes [41].

Recently, a plasma downramp along the driver's propagation direction (z) has been proposed to decrease the phase velocity of the wake from the driver's velocity sufficiently so as to trap plasma electrons [42–44] with ultrahigh brightness in a nonlinear wake [25]. If a small amplitude sinusoidal density modulation is superimposed on the downramp, the wake expands and shrinks periodically

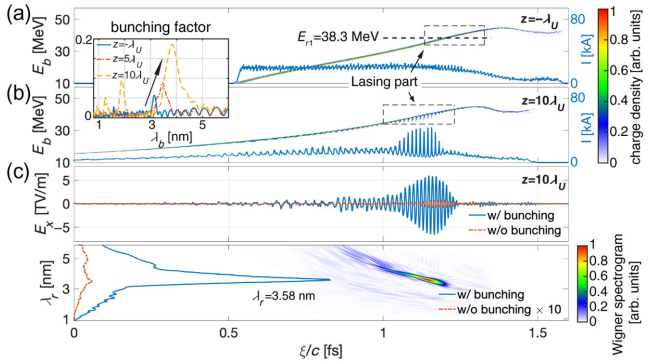

FIG. 2. Properties of the beam and attosecond pulse, along with the longitudinal phase space of the beam and its current profile (blue) when it exits the plasma (a) and when the radiation is saturated (b). The bunching factor at three different positions inside the undulator is shown in the inset where the growth and shift of the bunching factor can be seen. (c) On-axis electric field and its Wigner function when the radiation is saturated. Results when the prebunching is absent are also shown as a comparison. Note the beam moves from left to right.

thereby turning the electron injection on/off during the expansion/contraction while the downramp maps the discrete injection to different axial phases leading to a bunched current profile with a period that is significantly compressed compared to that of the density modulation [45]. In the illustration shown in Fig. 1(a), an electron beam driver excites a wake and injects an ultrabright beam bunched at $\lambda_b \approx 3.2$ nm in a premodulated plasma downramp. Due to the mapping between the electrons' initial axial position (z_i) and their final position (phase) inside the wake ($\xi \equiv ct - z$), electrons injected earlier are accelerated a longer distance and reside at the head of the beam, and thus there is a 30 MeV/fs linear energy chirp [25] along the beam at the end of the ramp as shown in Fig. 2(a).

As an example of an optical undulator we here employ an appropriately delayed linearly polarized CO_2 laser pulse with wavelength $\lambda_{CO_2} = 10$ μm and normalized vector potential $a_{CO_2} = \frac{eE_{CO_2}\lambda_{CO_2}}{2\pi mc^2} = 3.52$ collides with the bunched beam as it exits the downramp, where E_{CO_2} is the laser's electric field. Such a laser pulse is equivalent to a magnet undulator with $\lambda_U = 5$ μm and $K = 3.52$, where $K = \frac{eB_U\lambda_U}{2\pi mc}$ is the undulator normalized vector potential amplitude and B_U is the magnetic field on-axis. The electrons with energy $\gamma_b mc^2$ oscillate along the laser polarization direction (x) with an amplitude $\frac{K\lambda_U}{2\pi\gamma_b}$ and radiate. The resonance condition gives the radiation wavelength as [11–13]

$$\lambda_r = \frac{\lambda_U}{2q\gamma_b^2}\left(1 + \frac{K^2}{2}\right), \tag{1}$$

where q is the harmonic number. For a prebunched beam with wavelength $\lambda_b = 3.2$ nm and $q = 1$, electrons with energy $\gamma_{r1} \approx 75$ (37.5 MeV) radiate superradiantly while others radiate incoherently. Thus, these resonant electrons can develop the FEL instability much faster. This is clearly seen in Figs. 2(a) and 2(b) where the electron beam's $(p_z, \frac{\xi}{c})$ phase space and axial current profile are shown as the beam enters the undulator and after saturation. In Fig. 2(b), the large current modulation and corresponding loss of beam energy are clearly seen only for the part of the beam near the resonant energy. The distribution of the electrons and the radiation intensity when it saturates are shown in Fig. 1(b), where most electrons have slipped to the positions where the radiation intensity is close to zero.

The bunching factor of the lasing part of the beam, $b = |\sum_{j=1}^{N_b} \exp(ikz_j)|/N_b$, grows from an initial value of 0.06 to 0.19. Here, $N_b \approx 2.3 \times 10^7$ is the total number of electrons in the region encompassed by the dashed rectangle in Figs. 2(a) and 2(b). The on-axis electric field of the radiation and its Wigner function are shown in Fig. 2(c). It can be seen that a 3.58 nm radiation pulse with 7.1 TV/m peak field, 7.6 GW peak power, and 96.2 as the full width at half maximum (FWHM) duration (corresponding to 0.64×10^{10} 0.35 keV photons) is generated. The radiated pulse has a −5.34 nm/fs chirp which is caused by the chirp of the beam, i.e., $\frac{\Delta\lambda_r}{\lambda_r} \approx -2\frac{\Delta\gamma_b}{\gamma_b}$. The FWHM spectral width is 66 eV which can support a Fourier transform limited pulse with 27.4 as duration [46–48]. For comparison, the radiation pulse and its spectra when the prebunching is absent are also shown in Fig. 2(c). Without prebunching, different parts of the beam grow from noise independently; thus, the field is weak, and the spectrum is broad [49].

Due to the ultrahigh focusing gradient inside the plasma wake, the output beam is tightly focused to a 34 nm spot size with a peak density of $n_b \approx 5.9 \times 10^{22}$ cm^{-3}. Such a high-density beam can drive the FEL instability with a normalized growth rate defined by the Pierce parameter [11–13] which for the parameters simulated can be as large as $\rho = (\frac{e^2K^2[JJ]^2n_b}{32\epsilon_0\gamma_{r1}^3mc^2k_U^2})^{1/3} \approx 0.09$, which is orders of magnetic higher than that in rf accelerator-based XFELs (∼0.001). The corresponding gain length is $L_g = \frac{\lambda_U}{4\pi\sqrt{3}\rho} \approx 2.6$ μm which is much less than the undulator period. Here ϵ_0 is the vacuum permittivity and $[JJ] = 0.772$ is the coupling factor between the electron beam and the field [11–13]. Due to its high density and low energy, the plasma oscillations between the current peaks of the beam occur on a length that is comparable to the gain length ($k_{pb}^{-1} \approx 4.9$ μm) and thus contribute to the instability. The FEL instability is in the transition between the Compton ($k_{pb}^{-1} \ll L_g$) and the Raman regime ($k_{pb}^{-1} \gg L_g$) [50].

Only electrons with energies corresponding with resonant frequencies inside the gain bandwidth can contribute to the radiation, thus the duration of the radiation pulse can be estimated as $\sigma_\tau \sim \frac{\rho}{(d\gamma_b/dt)/\gamma_b}$. The spectra as a function of propagation distance found in the inset of Fig. 2 show the

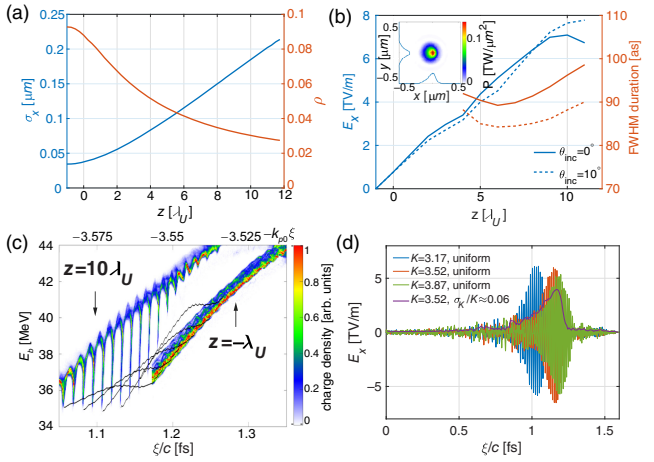

FIG. 3. Attosecond pulse generation inside an optical undulator. (a) Evolution of the beam spot size (blue) and the growth rate (red) of the instability. (b) Evolution of radiation field amplitude and its duration. Inset shows the power density distribution at its peak ($t = 1.172$ fs, $z = 10\lambda_U$) and the lineouts. A case where the CO_2 laser collides with the beam at 10° angle is shown to demonstrate the robustness of this scheme. Note that the intensity of the laser is decreased ($a_U = 3.51$) to compensate for the wavelength change due to the angle. (c) Energy loss and slippage of the lasing electrons where the black lines show the trajectories of electrons that lose a significant amount of energy. (d) The radiation pulses resulting from fluctuations of K.

bunching wavelength of the lasing electrons moves from initially 3.15 to 3.84 nm at saturation. This shift is mainly ascribed to the microbunching decompression of a chirped beam in an undulator since the high-energy electrons move faster than low-energy electrons (see Appendix B).

As the beam exits the plasma and expands inside the laser pulse, its spot size increases and thus the density decreases. This leads to a decrease in the Pierce parameter from $\rho \approx 0.09$ to 0.03 in ten undulator periods as shown in Fig. 3(a) while the FEL instability grows to saturation during this time as shown in Fig. 3(b). The longitudinal phase space of the lasing part of the beam is shown for $z = -\lambda_U$ and $10\lambda_U$ in Fig. 3(c). The electrons that lose energies are initially separated by a radiation wavelength and each electron loses as much as 11% of their initial energy (4.5 MeV). The trajectory of several selected electrons is also shown illustrating that the rate of energy loss varies across the beam and in time. As can be seen, the position of the beam at $z = -\lambda_U$ and $10\lambda_U$ has slipped due to the well-known phase slippage in the FEL instability. Figure 3(b) shows the evolution of the radiation field and its duration. The field grows roughly linearly and not exponentially since the transverse expansion of the beam leads to a continuously decreasing growth rate (see Appendix C) and then saturates. The pulse duration starts to increase after six periods because of the slippage. The transverse distribution of the radiation power density is shown in the inset with $\sigma_{x,y} \approx 80$ nm. The absence of the transverse focusing force along the optical undulator allows the beam to be incident with a large angle θ_{inc}, which only leads to a decrease of the undulator period as $\lambda_U \frac{1+\cos\theta_{inc}}{2}$. An example with $\theta_{inc} = 10°$ is shown in Fig. 3(b) where a similar radiation pulse is produced.

In reality, the intensity of the optical undulator may fluctuate. Two types of fluctuations are considered in Fig. 3(d). In the first, K is uniform but there is a shot-to-shot variation of 10% about a mean value. For this case, the produced radiation pulses are similar except they slip slightly in time. The self-selection mechanism ensures the optical undulator with different K can find resonant electrons to lase. In the second, the K has random fluctuations along z within the pulse. However, the large gain bandwidth of the instability in the proposed concept which is roughly equal to the Pierce parameter ($\rho \approx 0.09$) can tolerate a large fluctuation of the undulator intensity within the pulse. The peak field of the averaged radiation envelope from 10 shots is only reduced to 66% of the original value when $\sigma_K/K \approx 0.06$.

In the above results, the maximum energy of the beam is close to the resonant energy E_{r1} of the fundamental bunching wavelength, and an isolated attosecond pulse with the bunching wavelength is generated. If the beam is accelerated further inside the plasma, it can cover energies that are not only resonant with the fundamental but also resonant with harmonics of the prebunched wavelength. Depending on the range of energies of the beam different regions of the beam will be resonant with different harmonics and radiate independently to generate several fully coherent attosecond pulses with multiples of the fundamental wavelength and controllable separations on an subfemtosecond scale. We accelerate the electron beam further in a density plateau of a length of 12 μm that follows the ramp to a maximum energy of 57 MeV, which not only covers the fundamental but also the second ($E_{r2} = 51.1$ MeV) harmonics. After a collision with the same optical undulator, two attosecond pulses (93 and 30 as) with different wavelengths (4.0 and 1.8 nm) separated

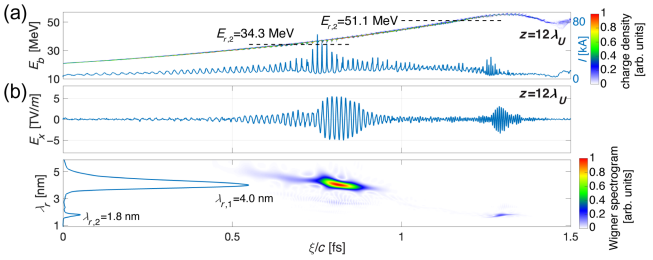

FIG. 4. Generation of two attosecond pulses with different wavelengths. (a) Longitudinal phase space at $z = 12\lambda_U$ and the current profile of the beam. The resonant parts of the two radiation pulses are shown by black dashed lines. (b) On-axis electric field and its Wigner function.

by 477 as are produced as shown in Fig. 4. The wavelengths are not exact harmonics because the shift of the fundamental wavelength during the propagation is more than that of the second harmonic (see Appendix B). Such a sequence of two-colored pulses can enable attosecond pump and attosecond probe studies or probe an ultrafast process to obtain a "movie" with attosecond resolution in a single shot.

The properties of coherent, attosecond x-ray pulses generated from the interaction of a highly chirped and prebunched beam with an optical undulator can be tuned easily. The duration of each pulse and their separation are inversely proportional to the local chirp of the beam, which can be controlled by the gradient of the ramp [25,45] while the pulse duration can also be tuned by the growth rate of the instability. An example, where a beam with a larger energy chirp generates 38 and 15 as pulses with 66 as separation is shown in Appendix D. A nonlinear downramp can lead to a nonlinear energy chirp, which can control the colors of the pulses independently. By controlling the acceleration distance inside the plasma, the energy distribution of the beam can be varied which determines the number of the generated pulses. Extensive simulation scans have found that the current of the self-injected beam produced from downramp injection is around half of the drive beam current [25,27,28], thus the peak power of the radiation can be increased if a drive beam with a higher current is used. The wavelength of the radiation which is approximately equal to the bunching wavelength of the electron beam can be continuously tuned between ∼10 and ∼0.1 nm by adjusting the ramp gradient and/or the plasma density modulation period [45].

A short and tightly focused GeV-class electron beam driver is used in the above simulations to effectively excite a nonlinear plasma wake and produce prebunched beams. Adequate electron beams might exist in the future at both FACET-II [51] and FlashForward [52]. However, such a short electron beam driver could be produced in a separate laser plasma accelerator stage as demonstrated in staged experiments [53–56]. Alternatively, intense laser pulses could replace the electron beam drivers and be used directly to produce prebunched beams which leads to simpler design of the proposed concept [45]. Although there are only a few adequate conventional electron beam sources, there are numerous hundred TW class laser systems in the world. Thus, there are many facilities that could explore this concept.

The above radiation generation scheme will lead to a more compact XFEL compared to other PBA-based schemes [20,21,24] that nevertheless use a conventional magnetic undulator and multiple transport components. The proposed scheme is free of the need to transport and match the beam to the undulator since the beam interacts with the optical undulator immediately after the plasma. It can tolerate large transverse angular and position jitters since the undulator is only tens of optical wavelengths long and has a much larger spot size than the electron beam. Since this process automatically selects the lasing portion from the whole beam, it can tolerate a beam with a large energy spread or significant shot-to-shot energy jitter as long as the resonant energy is covered by the beam. The large gain bandwidth of the FEL instability in the proposed concept which is roughly equal to the Pierce parameter ($\rho \approx 0.09$) can tolerate a large fluctuation of the optical undulator intensity. By utilizing ultrashort electron bunches produced from laser plasma accelerators [57] as drivers and laser pulses with micron wavelength as undulator, this scheme can be scaled to a hard x-ray regime to produce several attosecond pulses. These advantages make this ultracompact XFEL scheme particularly attractive.

This work was supported by the National Natural Science Foundation of China (NSFC) (No. 12375147 and No. 11921006) and the National Grand Instrument Project (No. 2019YFF01014400), Guangdong Provincial Science and Technology Plan Project (2021B0909050006) and Beijing Outstanding Young Scientist project, the Fundamental Research Funds for the Central Universities, Peking University, and the U.S. Department of Energy under Contracts No. DE-AC02-76SF00515 and No. DESC0010064, the U.S. National Science Foundation under Grants No. 2108970, and the DOE Scientific Discovery through Advanced Computing (SciDAC) program through a Fermi National Accelerator Laboratory (FNAL) subcontract No. 644405 and a Lawrence Berkeley National Laboratory (LBNL) subcontract No. 7350365:1. The simulations were performed on the resources of the National Energy Research Scientific Computing Center (NERSC), a U.S. Department of Energy Office of Science User Facility located at Lawrence Berkeley National Laboratory.

APPENDIX A: SIMULATION SETUP AND DATA ANALYSIS

1. Particle-in-cell (PIC) simulations

The simulations are carried out using the fully relativistic, electromagnetic particle-in-cell (PIC) code OSIRIS [29]. The injection of the bunched beam in a density modulated ramp is modeled in cylindrical geometry. A simulation window moving with a speed of light has dimensions of 13.5×14.4 μm with 18000×6144 cells in the z and r directions, respectively. This corresponds to cell sizes of $\Delta z = 0.75$ nm and $\Delta r = 2.34$ nm. The time step is $\Delta t = \frac{\Delta z}{2c} = 1.25$ as. There are eight macroparticles per cell to represent the plasma electrons and the beam electrons. A Maxwell solver with an extended stencil [30] (16 coefficients) is used to model the bunched beam generation with high fidelity [31]. The 1 GeV electron beam driver has a tri-Gaussian distribution with a spot size of 0.6 μm

($0.5\ k_{p0}^{-1}$), a duration of 0.84 μm ($0.7\ k_{p0}^{-1}$), and a 34 kA peak current. The plasma starts with a 30 μm ($25\ k_{p0}^{-1}$) sinusoidal upramp where the density increases from zero to $1.1n_{p0}$ ($n_{p0} = 1.97 \times 10^{19}\ \mathrm{cm}^{-3}$), then a 30 μm ($25\ k_{p0}^{-1}$) long plateau, then a 60 μm ($50\ k_{p0}^{-1}$) long downramp where the density is decreased linearly from $1.1n_{p0}$ to n_{p0}. A sinusoidal density modulation with 400 nm period and $0.002n_{p0}$ amplitude is superimposed along the ramp. An acceleration stage of length 12 μm ($10\ k_{p0}^{-1}$) is used in Fig. 4 to improve the electrons' energy while it is absent in Figs. 2 and 3. Results from a simulation conducted with a finer grid size ($\Delta z = 0.3$ nm and $\Delta r = 0.59$ nm) to resolve the second harmonic are shown in Fig. 4.

The distributions of the bunched beams generated from the $r - z$ simulations described above are interpolated onto 6D phase space by giving each particle a random phase in $x - y$ and $p_x - p_y$ space, respectively. Then these 6D phase space distributions are imported to full-3D PIC simulations where they interact with an optical undulator to generate attosecond pulses. For the case without bunching shown in Fig. 2(c), a random axial offset with 4 nm amplitude (slighter longer than the bunching wavelength) is added to the electrons, axial positions to eliminate the bunching. Since the beam energy varies significantly across the beam (from ∼10 to ∼60 MeV) and the growth rate of the instability is so large that the radiation grows significantly even in one undulator period, the generation of the radiation cannot be modeled using current major FEL codes, like GENESIS 1.3 [32]. We use PIC code OSIRIS to model this process in full 3D geometry. Such simulations require sufficient resolution to accurately model the bunching and x-ray wavelength. A simulation window moving with a speed of light has dimensions of $0.48 \times 1.2 \times 1.2\ \mu\mathrm{m}^3$ with $3200 \times 320 \times 320$ cells in the z, x, and y directions, respectively. This corresponds to cell sizes of $\Delta z = 0.15$ nm and $\Delta x = \Delta y = 3.75$ nm. The time step is $\Delta t = \frac{\Delta z}{2c} = 0.25$ as. A customized Maxwell solver with an extended stencil [30] (16 coefficients) is used to model the attosecond pulse generation with high fidelity [31]. The optical undulator is described by a prescribed 1D field profile, which is reasonable since its spot size is much larger than the transverse size of the simulation box. It starts with a profile as $a_{\mathrm{CO}_2}(k_{\mathrm{CO}_2} z - \omega_{\mathrm{CO}_2} t) \exp\left[-\frac{(k_{\mathrm{CO}_2} z - \omega_{\mathrm{CO}_2} t)^2}{2}\right]$ and then a constant envelope.

2. Data analysis

The Wigner distribution of the radiation electric field is obtained by using the "wvd" function provided by MATLAB. The one shown in Fig. 4(b) uses a Kaiser window with shape factor $\beta = 20$ and width 500.3 as (1001 data points) for the time domain and a Kaiser window with shape factor $\beta = 20$ and width 313 PHz (1001 data points) for the frequency domain to avoid the interference between the two attosecond pulses with different wavelengths.

APPENDIX B: THE DECOMPRESSION OF THE BEAM INSIDE THE UNDULATOR

As the electrons propagate inside the undulator, the relative slippage caused by their axial velocity difference may modify the bunching wavelength. In this section, we quantify this effect and compare it with the simulation results.

The average axial velocity of an electron inside a undulator is $\bar{\beta}_z = 1 - \frac{1}{2\gamma^2}(1 + K^2)$. Thus the slippage between two electrons with energy $\gamma_1 mc^2$ and $\gamma_2 mc^2$ when they propagate through N_U undulator periods is

$$\Delta s \approx N_U \lambda_U (\bar{\beta}_1 - \bar{\beta}_2) \approx 2N_U \lambda_r \frac{\gamma_2 - \gamma_1}{\gamma_1}, \tag{B1}$$

where $\frac{|\gamma_2 - \gamma_1|}{\gamma_1} \ll 1$ is assumed. We can rewrite this slippage as a function of the energy chirp of the beam, $(\mathrm{d}\gamma/\mathrm{d}\xi)$, as $\Delta s \approx 2N_U \lambda_r \frac{(\mathrm{d}\gamma/\mathrm{d}\xi)\Delta\xi}{\gamma_1}$, where $\Delta\xi$ is the axial separation of these two electrons. For the case studied in the main body, we consider two electrons that are initially separated by one bunching wavelength, their axial shift, which is also the shift of the bunching wavelength, can be written as

$$\Delta s = \Delta\lambda_b = \approx 2N_U \lambda_r^2 \frac{(\mathrm{d}\gamma/\mathrm{d}\xi)}{\gamma_1}. \tag{B2}$$

Substituting the parameters of Fig. 2 into the above formula ($\lambda_b \approx 3.2$ nm and the energy chirp is 30 MeV/fs) and noting the electrons at the front have higher energies, gives $\Delta\lambda_b\,[\mathrm{nm}] \approx 0.053N_U$. Thus the separation of the electrons increases as they propagate inside the undulator. After ten periods, the increase of the bunching wavelength is estimated to be $\Delta\lambda_b \approx 0.53$ nm which agrees well with the shift of the bunching wavelength as seen in the inset of Fig. 2 of the main text.

From Eq. (B2), we can also see the relative shift of the bunching wavelength which is defined as the ratio of the shifted wavelength to the wavelength that is smaller for high-order harmonics than that of the fundamental wavelength since this ratio is proportional to the wavelength and inversely proportional to the resonant energy, i.e., $\frac{\Delta\lambda_{b,q}}{\lambda_{b,q}} = 2N_U \frac{\mathrm{d}\gamma}{\mathrm{d}\xi}\frac{\lambda_{r,q}}{\gamma_q}$, where the subscript "q" indicates the q-th harmonics.

APPENDIX C: THE GROWTH OF THE RADIATION FIELD

We create an artificial zero emittance beam by setting the transverse momentum of the injected electrons to be zero and model its radiation generation inside the same optical undulator. In Fig. 5, the spot size evolution and radiation field growth are compared for the real injected beam from

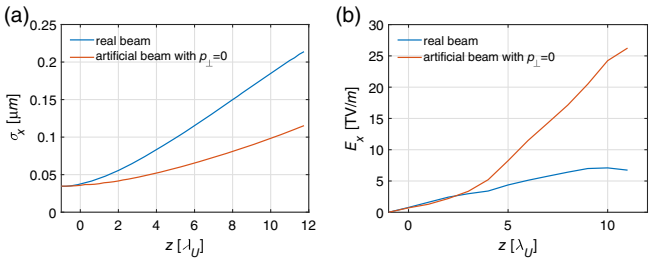

FIG. 5. Expansion of the electron beam and the growth of the radiation field for two cases. (a) Spot size evolution of the real beam and the artificial beam with $p_\perp = 0$. (b) Growth of the radiation field along the optical undulator for these two cases.

simulations and the zero emittance beam. The spot size of the artificial beam still grows even though its initial transverse momentum is zero, which is mainly caused by the space charge repulsion between the tightly focused electrons. The slow expansion of the artificial beam leads to a fast growth of the radiation field as shown in Fig. 5(b). Unlike the roughly linear growth in the real beam case, the radiation field in the artificial beam case grows closer to the exponential profile predicted by FEL theory. This comparison indicates that one important reason for the linear growth of the radiation field when the injected beam collides with an optical undulator is the transverse expansion of the electrons. At $z = 10\lambda_U$, the field of the radiation emitted by the artificial beam reaches ~24 TV/m, which is ~3 times higher than that of the real beam.

APPENDIX D: TUNING THE RADIATION PULSE DURATION BY CONTROLLING THE ENERGY CHIRP OF THE INJECTED BEAM

We show one example where the pulse duration of the radiation is reduced to a few tens of as by using an electron beam with a large energy chirp (146 MeV/fs). A density modulated plasma downramp with gradient $g = 5 \times 10^{-4}$ and period $\lambda_m = 1.2$ μm is used to inject a high-quality electron beam with a large energy chirp and a prebunched wavelength of $\lambda_b \approx 2.5$ nm. The compression factor of this ramp is around 480. The beam spot size and its slice energy spread are similar to that in the main body of the beam generated for $g = 0.002$ case while the average current of $I_b \approx 35$ kA is higher than for $g = 0.002$ case. We then collide this prebunched beam with a CO_2 laser pulse with $a_{CO_2} = 3.54$ to emit the attosecond radiation pulses. Three-dimensional OSIRIS simulations show two attosecond x-ray pulses are produced after six undulator period as shown in Fig. 6. The central wavelengths of the pulses are 2.76 and 1.45 nm. Their FWHM durations are 38 and 15 as while the separation is 66 as. The peak powers of these two pulses are 11 and 7.9 GW, which corresponds to 2.7×10^9 photons with 45 keV energy and 0.53×10^9 photons with 0.86 keV

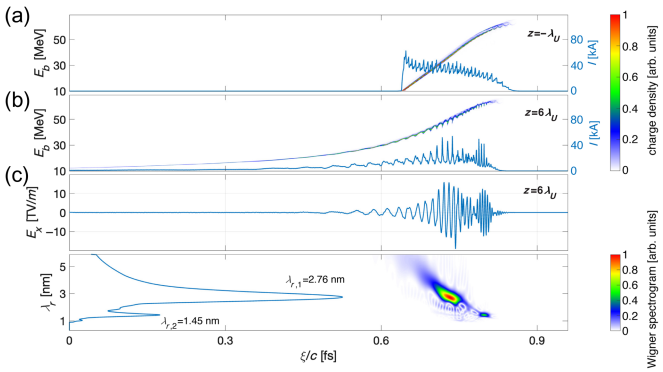

FIG. 6. Generation of two attosecond pulses with 38 and 15 as durations by using an electron beam with a large energy chirp. (a),(b) Longitudinal phase space of the prebunched beam and its current profile at $z = -\lambda_U$ (a) and $z = 6\lambda_U$ (b). (c) On-axis electric field and its Wigner function of the radiation at $z = 6\lambda_U$. Note the beam moves from left to right.

energy. The peak electric fields of these two pulses are 18 and 14 TV/m, respectively. Recall for $g = 0.002$, the central wavelengths were 4.0 and 1.8 nm, a separation of 477 as, and FWHM durations of 93 as and 30 as.

[1] P. B. Corkum and F. Krausz, Nat. Phys. **3**, 381 (2007).
[2] P. H. Bucksbaum, Science **317**, 766 (2007).
[3] F. Krausz and M. Ivanov, Rev. Mod. Phys. **81**, 163 (2009).
[4] F. Lépine, M. Y. Ivanov, and M. J. Vrakking, Nat. Photonics **8**, 195 (2014).
[5] F. Krausz and M. I. Stockman, Nat. Photonics **8**, 205 (2014).
[6] M. Nisoli, P. Decleva, F. Calegari, A. Palacios, and F. Martín, Chem. Rev. **117**, 10760 (2017).
[7] P. Agostini and L. F. DiMauro, Rep. Prog. Phys. **67**, 813 (2004).
[8] G. Sansone, L. Poletto, and M. Nisoli, Nat. Photonics **5**, 655 (2011).
[9] M. Chini, K. Zhao, and Z. Chang, Nat. Photonics **8**, 178 (2014).
[10] F. Quéré and C. Thaury, J. Phys. B **43**, 213001 (2010).
[11] E. Saldin, E. Schneidmiller, and M. V. Yurkov, *The Physics of Free Electron Lasers* (Springer Science & Business Media, Berlin, Germany, 1999).
[12] Z. Huang and K.-J. Kim, Phys. Rev. ST Accel. Beams **10**, 034801 (2007).
[13] C. Pellegrini, A. Marinelli, and S. Reiche, Rev. Mod. Phys. **88**, 015006 (2016).
[14] J. Duris, S. Li, T. Driver, E. G. Champenois, J. P. MacArthur, A. A. Lutman, Z. Zhang, P. Rosenberger, J. W. Aldrich, R. Coffee *et al.*, Nat. Photonics **14**, 30 (2020).
[15] T. Tajima and J. M. Dawson, Phys. Rev. Lett. **43**, 267 (1979).
[16] P. Chen, J. Dawson, R. W. Huff, and T. Katsouleas, Phys. Rev. Lett. **54**, 693 (1985).
[17] E. Esarey, C. B. Schroeder, and W. P. Leemans, Rev. Mod. Phys. **81**, 1229 (2009).

[18] C. Joshi, S. Corde, and W. Mori, Phys. Plasmas **27**, 070602 (2020).

[19] C. Emma, J. Van Tilborg, R. Assmann, S. Barber, A. Cianchi, S. Corde, M. Couprie, R. D'arcy, M. Ferrario, A. Habib *et al.*, High Power Laser Sci. Eng. **9**, e57 (2021).

[20] W. Wang, K. Feng, L. Ke, C. Yu, Y. Xu, R. Qi, Y. Chen, Z. Qin, Z. Zhang, M. Fang *et al.*, Nature (London) **595**, 516 (2021).

[21] R. Pompili, D. Alesini, M. Anania, S. Arjmand, M. Behtouei, M. Bellaveglia, A. Biagioni, B. Buonomo, F. Cardelli, M. Carpanese *et al.*, Nature (London) **605**, 659 (2022).

[22] M. Galletti, D. Alesini, M. P. Anania, S. Arjmand, M. Behtouei, M. Bellaveglia, A. Biagioni, B. Buonomo, F. Cardelli, M. Carpanese *et al.*, Phys. Rev. Lett. **129**, 234801 (2022).

[23] M. Labat, J. C. Cabadağ, A. Ghaith, A. Irman, A. Berlioux, P. Berteaud, F. Blache, S. Bock, F. Bouvet, F. Briquez *et al.*, Nat. Photonics **17**, 150 (2023).

[24] C. Emma, X. Xu, A. Fisher, R. Robles, J. MacArthur, J. Cryan, M. Hogan, P. Musumeci, G. White, and A. Marinelli, APL Photonics **6**, 076107 (2021).

[25] X. Xu, F. Li, W. An, T. Dalichaouch, P. Yu, W. Lu, C. Joshi, and W. Mori, Phys. Rev. Accel. Beams **20**, 111303 (2017).

[26] G. G. Manahan, A. Habib, P. Scherkl, P. Delinikolas, A. Beaton, A. Knetsch, O. Karger, G. Wittig, T. Heinemann, Z. Sheng *et al.*, Nat. Commun. **8**, 15705 (2017).

[27] T. Dalichaouch, X. Xu, F. Li, A. Tableman, F. Tsung, W. An, and W. Mori, Phys. Rev. Accel. Beams **23**, 021304 (2020).

[28] F. Li, T. N. Dalichaouch, J. R. Pierce, X. Xu, F. S. Tsung, W. Lu, C. Joshi, and W. B. Mori, Phys. Rev. Lett. **128**, 174803 (2022).

[29] A. Habib, G. Manahan, P. Scherkl, T. Heinemann, A. Sutherland, R. Altuiri, B. Alotaibi, M. Litos, J. Cary, T. Raubenheimer *et al.*, Nat. Commun. **14**, 1054 (2023).

[30] A. Gover, R. Ianconescu, A. Friedman, C. Emma, N. Sudar, P. Musumeci, and C. Pellegrini, Rev. Mod. Phys. **91**, 035003 (2019).

[31] S. Huang, Y. Ding, Y. Feng, E. Hemsing, Z. Huang, J. Krzywinski, A. Lutman, A. Marinelli, T. Maxwell, and D. Zhu, Phys. Rev. Lett. **119**, 154801 (2017).

[32] Z. Zhang, J. Duris, J. P. MacArthur, A. Zholents, Z. Huang, and A. Marinelli, New J. Phys. **22**, 083030 (2020).

[33] L. R. Elias, Phys. Rev. Lett. **42**, 977 (1979).

[34] A. Gover, C. Tang, and P. Sprangle, J. Appl. Phys. **53**, 124 (1982).

[35] K. Floettmann, Phys. Rev. ST Accel. Beams **17**, 054402 (2014).

[36] X. L. Xu, J. F. Hua, Y. P. Wu, C. J. Zhang, F. Li, Y. Wan, C.-H. Pai, W. Lu, W. An, P. Yu *et al.*, Phys. Rev. Lett. **116**, 124801 (2016).

[37] G. Mourou, B. Brocklesby, T. Tajima, and J. Limpert, Nat. Photonics **7**, 258 (2013).

[38] R. Fonseca *et al.*, Lect. Notes Comput. Sci. **2331**, 342 (2002).

[39] F. Li, P. Yu, X. Xu, F. Fiuza, V. K. Decyk, T. Dalichaouch, A. Davidson, A. Tableman, W. An, F. S. Tsung *et al.*, Comput. Phys. Commun. **214**, 6 (2017).

[40] X. Xu, F. Li, F. S. Tsung, T. N. Dalichaouch, W. An, H. Wen, V. K. Decyk, R. A. Fonseca, M. J. Hogan, and W. B. Mori, J. Comput. Phys. **413**, 109451 (2020).

[41] S. Reiche, Nucl. Instrum. Methods Phys. Res., Sect. A **429**, 243 (1999).

[42] T. Katsouleas, Phys. Rev. A **33**, 2056 (1986).

[43] H. Suk, N. Barov, J. B. Rosenzweig, and E. Esarey, Phys. Rev. Lett. **86**, 1011 (2001).

[44] S. Bulanov, N. Naumova, F. Pegoraro, and J. Sakai, Phys. Rev. E **58**, R5257 (1998).

[45] X. Xu, F. Li, F. S. Tsung, K. Miller, V. Yakimenko, M. J. Hogan, C. Joshi, and W. B. Mori, Nat. Commun. **13**, 3364 (2022).

[46] L. Poletto and F. Frassetto, J. Synchrotron Radiat. **25**, 52 (2018).

[47] S. Bajt, H. N. Chapman, A. Aquila, and E. Gullikson, J. Opt. Soc. Am. A **29**, 216 (2012).

[48] H. Li, J. MacArthur, S. Littleton, M. Dunne, Z. Huang, and D. Zhu, Phys. Rev. Lett. **129**, 213901 (2022).

[49] S. Krinsky and Z. Huang, Phys. Rev. ST Accel. Beams **6**, 050702 (2003).

[50] A. Gover and P. Sprangle, IEEE J. Quantum Electron. **17**, 1196 (1981).

[51] V. Yakimenko, L. Alsberg, E. Bong, G. Bouchard, C. Clarke, C. Emma, S. Green, C. Hast, M. J. Hogan, J. Seabury *et al.*, Phys. Rev. Accel. Beams **22**, 101301 (2019).

[52] R. D'Arcy, A. Aschikhin, S. Bohlen, G. Boyle, T. Brummer, J. Chappell, S. Diederichs, B. Foster, M. J. Garland, L. Goldberg *et al.*, Phil. Trans. R. Soc. A **377**, 20180392 (2019).

[53] J. Götzfried, A. Döpp, M. Gilljohann, F. Foerster, H. Ding, S. Schindler, G. Schilling, A. Buck, L. Veisz, and S. Karsch, Phys. Rev. X **10**, 041015 (2020).

[54] T. Kurz, T. Heinemann, M. Gilljohann, Y. Chang, J. Couperus Cabadag, A. Debus, O. Kononenko, R. Pausch, S. Schöbel, R. Assmann *et al.*, Nat. Commun. **12**, 2859 (2021).

[55] J. P. Couperus Cabadağ, R. Pausch, S. Schöbel, M. Bussmann, Y.-Y. Chang, S. Corde, A. Debus, H. Ding, A. Döpp, F. M. Foerster *et al.*, Phys. Rev. Res. **3**, L042005 (2021).

[56] F. Foerster, A. Döpp, F. Haberstroh, K. v. Grafenstein, D. Campbell, Y.-Y. Chang, S. Corde, J. C. Cabadağ, A. Debus, M. Gilljohann *et al.*, Phys. Rev. X **12**, 041016 (2022).

[57] M. Tooley, B. Ersfeld, S. Yoffe, A. Noble, E. Brunetti, Z. Sheng, M. Islam, and D. Jaroszynski, Phys. Rev. Lett. **119**, 044801 (2017).